Multiscale Heterogeneous Modeling with Surfacelets

Yan Wang[1] and David W. Rosen[2]

[1]Georgia Institute of Technology, yan.wang@me.gatech.edu
[2]Georgia Institute of Technology, david.rosen@me.gatech.edu

ABSTRACT

Computational design of structures and materials requires multiscale models to represent geometry and physical properties. In this paper, we propose a multiscale heterogeneous model, dual-Rep, to represent geometry and property distribution implicitly. A new basis function, called surfacelet, is proposed to capture boundary information more efficiently than traditional wavelets. Zoom operations are defined to support multiscale design. A method of materials model reconstruction from images is also developed.

Keywords: computational materials design, wavelet.
DOI: 10.3722/cadaps.2010.759-776

1 INTRODUCTION

In the most recent decade, computer-aided materials design has become a critical component of product design, since product innovation heavily depends on the availability of new materials. Future computer-aided design (CAD) systems should support multiscale geometry and materials modeling. There are challenges to represent structures with complex geometry and topology in materials design. For instance, super-porous structures exist in natural and man-made materials. The topology is much more complex than the regularly used engineering shapes. If we 'zoom in' to an even smaller scale, materials are no longer continuous and the geometry becomes the material structure. The heterogeneity of material properties needs to be modeled explicitly if we want to design materials with very fine-grained details. Existing CAD geometric modeling based on explicit and parametric representations is not efficient in specifying the complex topology.

In multiscale CAD systems, ranging from nano (10^{-9}~10^{-8} m), meso (~10^{-7} m), micro (10^{-6}~10^{-4} m), to macroscales (>10^{-3} m), the specifications of material compositions and distributions are as important as geometric shapes. At the traditional macroscale in engineering design, geometry and materials can be separately specified. However, at the micro- and meso-scales, material compositions become important in functional realization, such as in composites and functionally graded materials. At the nano-scale, geometry and material property become one-to-one correspondent to each other, such as in crystals and metal-organic frameworks. Therefore, we need a concise and precise form to capture material compositions along with geometry so that engineers can design materials in an interactive environment.

Even though multi-resolution geometry representations (e.g., subdivision and wavelets) have been developed, the geometric information is only at the same length scale; from this information, representations at different levels of detail (LOD) can be generated. The major difference between *multiscale* and *multi-resolution* modeling is that in a multi-resolution environment, the complete model information is available at the highest resolution, while in multiscale modeling, the highest resolution need not be generated, except when and where it may be needed. For instance, a multiscale model does not require the entire Boeing 787 airplane model to be available at the atomic scale if one component is required at this scale. Instead, in a multiscale environment, it is necessary to render the model at a specified scale when and where a specified region of a model can be rendered at a desired scale for a specific purpose, such as visualization, finite-element analysis, or manufacturing process planning [1].

In this paper, we propose a new multiscale geometric and materials modeling method that uses an implicit representation to efficiently captures internal and boundary information. This new approach can effectively represent multiscale complex structures as well as material compositions and distributions. It serves as the foundation for modeling structure-property relationships for materials design. We call our modeling approach *dual representation* or *dual-Rep*, since it represents both internal and boundary distributions of materials in a unified implicit form. This new model is proposed to support the multiscale zoom process. Fig. 1 illustrates how such a zoom process is important in representing multiscale materials such as bone structures. The external boundaries can be represented as continuous 2D red curves in Fig. 1-(a). As we zoom in, the zero-width boundary becomes a domain with internal material distributions, as in Fig. 1-(b). In other words, explicit boundaries with zero width in the previous scale now become continuous distributions of materials with fine-grained features inside the boundary structures themselves. On the other hand, when zoomed in, it becomes more convenient to model some internal regions where relatively high gradients of distributions exist (i.e., with large contrast between black and white colors in the images) by boundary representation, as in Fig. 1-(c). With further magnification of continuous regions to the atomic level, the polycrystalline structure emerges, where grain boundaries and defects can be modeled efficiently with boundary representations again, as in Fig. 1-(d). Therefore, boundary and internal are complementary structures. The purpose of the dual-Rep model is to support such role exchanges of boundary and internal structures at different length scales. The enabling core part of the dual-Rep model is a new basis function called surfacelet.

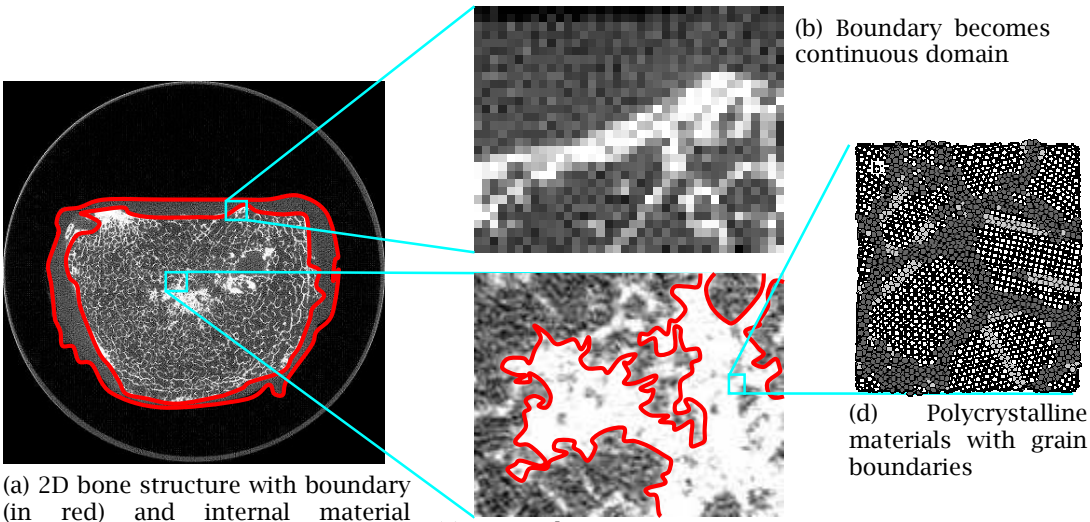

Fig. 1: An illustration of dual-Rep model for multiscale geometry and materials modeling with boundary and internal structures exchanges at difference scales.

In the remainder of the paper, we gave a brief background review of relevant work in Section 2. The proposed surfacelet functions are introduced in Section 3. The dual-Rep multiscale heterogeneous model based on surfacelets is described in Section 4. Finally, a model reconstruction approach is described in Section 5.

2 BACKGROUND

In this section, we give a brief overview of relevant work to our proposed multiscale materials modeling approach, including heterogeneous modeling in Section 2.1 and multi-resolution geometry representations in Section 2.2.

2.1 Heterogeneous Modeling

Heterogeneous modeling usually denotes the modeling of geometry and material composition. Some researchers may include non-manifold topology under the term, which we allow, but do not emphasize. Two general approaches to heterogeneous modeling have been proposed [2]: discretized and non-discretized approaches. In the first category, materials and geometry are modeled separately, such as mesh-based and voxel-based methods, where geometry is approximated by volume meshes or voxels [3], and material distributions are determined by topology optimization or numerical interpolation from control features [4]. Other researchers applied voxel-based representations that utilized spatial occupancy enumeration of part geometry. Again, material composition information was applied to either individual voxels or interpolated over sets of voxels using a part's bounding surface [5]. General cellular decompositions have also received considerable attention [6]. A general cellular decomposition-based approach integrated physical property distributions into the geometry+material model [7] that others have investigated. Some researchers have generalized the cellular modeling approach to include manufacturing process-related Local Composition Control (LCC) elements [8].

In non-discretized approaches, some researchers have separated the representation of material compositions and properties from the underlying part geometry [9]. Others have utilized implicit modeling approaches, which has advantages in that a common mathematical model is used for both geometry and material composition [10]. Shapiro and coworkers have applied the theory of R-functions to show how material composition [11] can be performed using implicit modeling approaches. The advantage of their approach is the unifying nature of implicit modeling to model geometry, material composition, and distributions of any physically meaningful quantity throughout a part. A different group proposed a method based on hypertextures [12] that provides more intuitive user controls, according to the developers. Similar to the implicit modeling approaches, material compositions were specified on part surfaces and similar types of distance measures were used to compute compositions internal to parts.

The limitation of all work described here is that the models are not multiscale; at best some can be called multi-resolution, specifically the methods in the first general approach based on geometric decompositions. Even then, the resolutions are limited to the overall part geometry and the particular decomposition into cells, voxels, or mesh elements. In contrast, our proposed approach is both multiscale and multi-resolution, where part representations can be generated at the desired size scale and resolution.

2.2 Multi-resolution Geometry Representations

There have been various efforts on multi-resolution geometry representation. The basic ideas are based on functional approximations in the Hilbert space. Choosing appropriate basis functions that have multi-resolution properties is the core research issue. The most studied ones are B-splines and wavelets.

2.2.1 B-Spline

B-spline is widely used as the basis function in geometric modeling and simulation. Through knot insertion and degree elevation [13], B-spline curves and surfaces can be refined with more control points introduced. Reversely, control points can be reduced in approximations.

A more general multi-resolution representation is subdivision curves and surfaces [14, 15], which are based on the B-spline refinability. That is, the B-spline basis function can be written as a linear combination of the translated and dilated copies of itself. Therefore, by recursively refining control points based on some topological and geometric rules, the control polygon or mesh converges to the limit B-spline curve or surface. Recently, more subdivision schemes have been developed for surfaces, such as Loop [16], Butterfly [17], $\sqrt{3}$ [18], $\sqrt{2}$ [19], etc., with carefully chosen subdivision rules.

2.2.2 Wavelets

In the domain of 2D shape representations, wavelets are among the most popular multi-resolution representations. Similar to Fourier analysis, wavelet analysis is to represent and approximate signals (or functions in general) with orthogonal or non-orthogonal basis functions. Both methods can be used to uncover frequency components of signals. Both can be used to represent multi-resolution subspaces and fast algorithms are available for both. However, instead of sinusoidal functions in Fourier analysis, the functional space for wavelet analysis is decomposed based on a scaling function $\varphi(t)$ and a wavelet function $\psi(t)$ with one dimensional variable t for multi-resolution analysis.

Wavelets are self-similar and can be scaled up and down. More specifically, the wavelet function

$$\psi_{a,b}(t) = a^{-1/2}\psi\left(a^{-1}(t-b)\right) \tag{0.1}$$

is scaled by a scaling (dilation) factor a and translated by a translation factor b. Although certain forms (e.g. Haar, Daubechies, Morlet, etc.) have been used extensively, $\psi(t)$ is actually general and can be customized for specific problems. Similar operations can be applied to scaling functions. The most important feature of wavelets is that they are localized in both real (time) and reciprocal (frequency) spaces due to the property of regularity and vanishing moments. With these properties, wavelets together with scaling functions can be used to approximate signals and functions in a compact form (compared to the traditional Fourier analysis), with local features represented more efficiently. Wavelets provide a general approach for multi-resolution functional analysis.

In geometric modeling domain, the wavelet transforms were used to describe planar curves with multiple resolutions [20]. Combining subdivision and lifting, a so-called normal multi-resolution approximation was developed to interpolate curves and surfaces [21]. Some new wavelets have also been constructed to represent geometries. For instance, Wang et al. [22, 23] developed a translation-invariant B-spline wavelet function for curve representation, which can be computed recursively with differential operations.

The above different multi-resolution modeling approaches capture geometric information in different levels of detail. However, they do not meet the requirement of multiscale design scenarios, where geometric information as well as material properties should be captured in a way so that users can retrieve either low-granularity global structures or high-granularity local information without rendering the global picture with the greatest details.

Our proposed multiscale representation of geometry and materials is based on a hybrid approach of implicit and boundary representations. The general idea is to represent materials distribution in a domain and its boundary with a combination of two types of basis functions. While regular wavelets can be used in internal distributions, a new basis function is introduced to model materials distributions in boundaries, which is called *surfacelet*. It is a generalization of ridgelet and curvelet, as introduced in the next section.

2.2.3 Wedgelet, Curvelets, and Surflet

Wavelets perform well for objects with point singularities in dimension 1. However they are not effective in dealing with edge discontinuities in dimension 2. Several so-called directional wavelet approaches have been proposed to solve this issue, including wedgelet [24] and curvelet [25], as well as their close relatives such as ridgelet [26], contourlet [27], beamlet [28], and platelet [29].

The wedgelet approach partitions 2D space into squares as building blocks which have line segments. 2D images then can be approximated by a collection of specifically chosen wedgelets. The curvelet function is an extension of the standard wavelet function, which combines the concepts of neural networks, Radon transform, and wavelets. It was developed to compress images containing

continuous line or curve segments, where the standard wavelets are not efficient. The idea of the curvelet was originally started as ridgelet, where an angular element θ is introduced in the wavelet function as

$$\psi_{a,b,\theta}(\mathbf{r}) = \psi_{a,b}(x\cos\theta + y\sin\theta) = a^{-1/2}\psi\left(a^{-1}(x\cos\theta + y\sin\theta - b)\right) \tag{0.2}$$

so that the parameters include scaling, translation, and orientation. Later, curvelet was constructed in the Fourier space in order to have better controls of resolution in the frequency domain. With the multi-resolution deployment of ridgelets, a parabolic scaling constraint of width ≈ length^2 can be introduced so that curvelets are no longer lines with infinite lengths. If wavelets can be thought of as "fat" points with certain widths of local support, curvelets are "fat" needles where orientation information can be captured.

In 3D analysis, Ying et al. [30] extended 2D curvelet transform to 3D with similar frequency space tilings. Similarly, Lu and Do [31] extended contourlets to three dimensions in a discrete space. Chandrasekaran et al. [32] extended wedgelets to high-dimensional space and approximate functions with polynomial building blocks, called surflets, instead of linear building blocks in wedgelets.

In this paper, we propose a new modeling approach to capture multiscale material distributions with a new surfacelet basis function. The proposed surfacelet can be viewed as a 3D generalization of the above directional wavelets. Also different from the purpose of the above efforts, which is to develop efficient approaches to represent and compress edge and surface singularities in 2D or 3D images in the format of pixels or voxels, we are interested in modeling both continuous distributions and surface singularities efficiently in a unified implicit form. In contrast to the above directional wavelet bases which are constructed in the Fourier domain, we would like to have direct controls in Euclidean space.

In order to support dual-Rep that allows for multiscale materials representation, a mixture of wavelet and surfacelet basis functions is chosen. Wavelet basis functions are used for continuous distributions, whereas surfacelet basis functions are used for surface singularities or boundaries. This approach enables us to capture both internal and boundary domains in a unified form so that seamless zoom operations between scales can be performed.

Our new basis function of surfacelets is a generalization of ridgelets. In the traditional ridgelets, line or plane-type boundaries can be represented efficiently. However, its support is not localized along the ridge direction, where $x\cos\theta + y\sin\theta$ is kept constant. Therefore, partitioning of the Euclidean space into smaller domains is required in the cases that boundaries are deviated far from linear singularities. As a result, artificially discontinuous boundaries may be introduced. Our new surfacelet functions generalize the shape singularities to higher orders such as quadratic surfaces. This allows for more flexibilities of boundary representation. The surfacelet is described in Section 3.

3 SURFACELET

We need to represent both internal and boundary material distributions in multiscale and multi-resolution modeling. The exchange between boundaries and internal structures such as the ones in Fig. 1 cannot be captured efficiently in the forms of regular wavelets or splines. Therefore, a different approach is required. Boundaries can be viewed as surface singularities that are discontinuous in one direction while continuous in other two in 3D space. They can be represented locally as planes, cylinders, ellipsoids, etc. Therefore, we propose surfacelet basis functions as building blocks of boundaries in multiscale modeling.

We define a general surfacelet basis function as

$$\psi_{a,b,\mathbf{p}}(\mathbf{r}) = a^{-1/2}\psi\left(a^{-1}\rho_{b,\mathbf{p}}(\mathbf{r})\right) \tag{0.3}$$

where $\mathbf{r} = (x, y, z)$ is the location in the domain Ω in the Euclidean space, $\psi : \mathbb{R} \to \mathbb{R}$ is a wavelet function, $a \in \mathbb{R}^+$ is a non-negative scaling factor, $\rho_{b,\mathbf{p}} : \mathbb{R}^3 \to \mathbb{R}$ is a surface function so that $\rho_{b,\mathbf{p}}(x, y, z) = 0$ implicitly defines a surface, with the translation factor $b \in \mathbb{R}$ and the shape parameter

vector $\mathbf{p} \in \mathbb{R}^m$ determining the location and shape of surface singularity respectively. Particularly, a 3D ridgelet that represents plane singularities is defined as

$$\psi_{a,b,\alpha,\beta}(\mathbf{r}) = a^{-1/2}\psi\left(a^{-1}\left(\cos\beta\cos\alpha\cdot x+\cos\beta\sin\alpha\cdot y+\sin\beta\cdot z-b\right)\right) \tag{0.4}$$

where $\alpha \in [0, 2\pi)$ and $\beta \in [-\pi/2, \pi/2]$ are angular parameters corresponding to rotations around z- and y-axes in the Euclidean space. Here the shape parameter vector is $\mathbf{p} = (\alpha, \beta)$. Similarly, a surfacelet that represents cylindrical singularities can be defined as

$$\psi_{a,b,\alpha,\beta,r_1,r_2}(\mathbf{r}) = a^{-1/2}\psi\left(a^{-1}\left[r_1\left(\cos\beta\cos\alpha\cdot x+\cos\beta\sin\alpha\cdot y+\sin\beta\cdot z-b\right)^2+r_2\left(-\sin\alpha\cdot x+\cos\alpha\cdot y\right)^2\right]\right) \tag{0.5}$$

A surfacelet that represents ellipsoidal singularities is defined as

$$\psi_{a,b,\alpha,\beta,r_1,r_2,r_3}(\mathbf{r}) = a^{-1/2}\psi\left(a^{-1}\left[\begin{array}{l} r_1\left(\cos\beta\cos\alpha\cdot x+\cos\beta\sin\alpha\cdot y+\sin\beta\cdot z-b\right)^2+r_2\left(-\sin\alpha\cdot x+\cos\alpha\cdot y\right)^2 \\ +r_3\left(-\sin\beta\cos\alpha\cdot x+\sin\beta\sin\alpha\cdot y+\cos\beta\cdot z\right)^2\end{array}\right]\right) \tag{0.6}$$

The isosurfaces of these three surfacelets for plane, cylindrical, and ellipsoidal singularities are shown in Fig. 2, where the Mexican hat basis

$$\psi(t) = (2\pi)^{-1/2}\sigma^{-3}\left(1-t^2\sigma^{-2}\right)e^{-t^2\sigma^{-2}/2} \tag{0.7}$$

is applied and $\sigma = 0.8$.

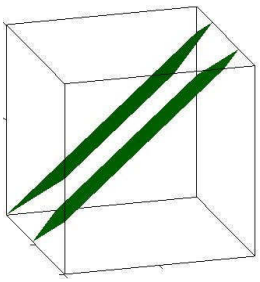

(a) 3D ridgelet ($a = 0.2$, $b = 0.1$, $\alpha = 11\pi/6$,

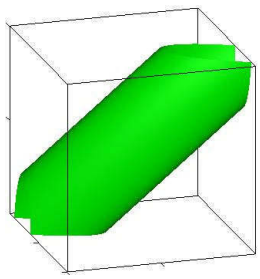

(b) Cylindrical surfacelet ($a = 0.2$, $b = 0.1$, $\alpha = 11\pi/6$, $\beta = \pi/4$, $r_1 = 1$, $r_2 = 4$)

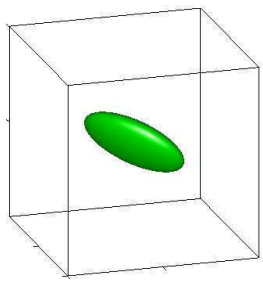

(c) Ellipsoidal surfacelet ($a = 0.2$, $b = 0.1$, $\alpha = 11\pi/6$, $\beta = \pi/4$, $r_1 = 1$, $r_2 = 4$, $r_3 = 9$)

Fig. 2: Isosurfaces of surfacelets.

The parameters of surfacelets can be geometrically interpreted as follows. For 3D ridgelets as in Fig. 3-(a), any point on a plane $\cos\beta\cos\alpha\cdot x+\cos\beta\sin\alpha\cdot y+\sin\beta\cdot z = t$ has the same evaluation of the wavelet function $\psi\left(a^{-1}(t-b)\right)$. Therefore, the isosurfaces of Eqn.(0.4) are planes. Similarly, for cylindrical surfacelets in Fig. 3-(b), all points on a cylinder $r_1\left(\cos\beta\cos\alpha\cdot x+\cos\beta\sin\alpha\cdot y+\sin\beta\cdot z-b\right)^2+r_2\left(-\sin\alpha\cdot x+\cos\alpha\cdot y\right)^2 = r_0^2$ have the same evaluation of wavelet functions in Eqn.(0.5). For ellipsoidal surfaces in Fig. 3-(c), all points on the ellipsoid $r_1\left(\cos\beta\cos\alpha\cdot x+\cos\beta\sin\alpha\cdot y+\sin\beta\cdot z-b\right)^2+r_2\left(-\sin\alpha\cdot x+\cos\alpha\cdot y\right)^2+r_3\left(-\sin\beta\cos\alpha\cdot x+\sin\beta\sin\alpha\cdot y+\cos\beta\cdot z\right)^2 = r_0^2$ have the same evaluation in Eqn.(0.6).

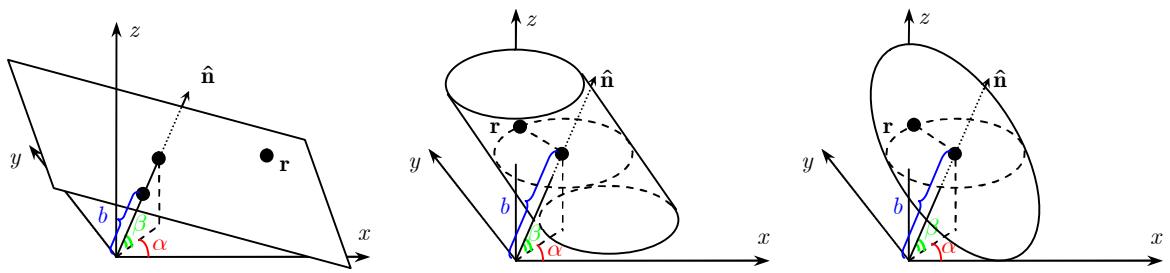

(a) 3D ridgelet (b) Cylindrical surfacelet (c) Ellipsoidal surfacelet

Fig. 3: Geometric interpretation of surfacelets.

Let $\hat{z}(\omega)$ denote the Fourier transform of $z(t)$ and $\bar{z}$ denote the complex conjugate of z. If $\psi(t)$'s are chosen such that the Parseval relationships

$$\int_{-\infty}^{\infty} \psi(t)\bar{\psi}(t)dt = \frac{1}{2\pi}\int_{-\infty}^{\infty} \hat{\psi}(\omega)\bar{\hat{\psi}}(\omega)d\omega \tag{0.8}$$

and the admissibility condition

$$\int_{-\infty}^{\infty} \left|\hat{\psi}(\omega)\right|^2 |\omega|^{-1} d\omega = 1 \tag{0.9}$$

are satisfied, based on the generic surfacelet basis function in Eqn.(0.3), an L^2 function $f(\mathbf{r})$ can be reproduced by

$$f(\mathbf{r}) = \int_{-\infty}^{\infty}\int_{\mathbf{p}}\int_{0}^{\infty} \Psi_{a,b,\mathbf{p}}\psi_{a,b,\mathbf{p}}(\mathbf{r})da\,d\mathbf{p}db \tag{0.10}$$

where

$$\Psi_{a,b,\mathbf{p}} = \int_{\mathbb{R}^3} f(\mathbf{r})\bar{\psi}_{a,b,\mathbf{p}}(\mathbf{r})d\mathbf{r} \tag{0.11}$$

For the 3D ridgelet in Eqn.(0.4), the surfacelet coefficients $\Psi_{a,b,\alpha,\beta}$'s can be efficiently calculated in the Fourier domain, since

$$\Psi_{a,b,\alpha,\beta} = \int_{\mathbb{R}^3} \bar{\psi}_{a,b,\alpha,\beta}(\mathbf{r})f(\mathbf{r})d\mathbf{r} = \frac{1}{2\pi}\int \bar{\hat{\psi}}_{a,b,\alpha,\beta}(\xi)\hat{f}(\xi)d\xi \tag{0.12}$$

as the result of Eqn.(0.8). We further convert the Cartesian coordinate ξ to the spherical coordinate. Let $\mathbf{u} = (\cos\beta\cos\alpha, \cos\beta\sin\alpha, \sin\beta)$, $\xi = (\lambda\cos\beta\cos\alpha, \lambda\cos\beta\sin\alpha, \lambda\sin\beta) = \lambda\mathbf{u}$, and $a^{-1}(\mathbf{u}\cdot\mathbf{r} - b) = t$. Then

$$\begin{aligned}\hat{\psi}_{a,b,\alpha,\beta}(\xi) &= \int a^{-1/2}\psi\left(a^{-1}(\mathbf{u}\cdot\mathbf{r} - b)\right)e^{-i\lambda\mathbf{u}\cdot\mathbf{r}}d\mathbf{r} = \int a^{-1/2}\psi(t)e^{-i\lambda(at+b)}d(at) = a^{1/2}e^{-i\lambda b}\int \psi(t)e^{-ia\lambda t}dt \\ &= a^{1/2}e^{-i\lambda b}\hat{\psi}(a\lambda)\end{aligned}$$

Therefore, for some specific values of α and β, we have

$$\Psi_{a,b,\alpha,\beta} = \frac{1}{2\pi}\int a^{1/2}\bar{\hat{\psi}}(a\lambda)e^{-i\lambda b}\hat{f}(\xi)d\lambda \tag{0.13}$$

The 3D ridgelet coefficient $\Psi_{a,b,\alpha,\beta}$ thus can be obtained by the one dimensional inverse Fourier transform of $\hat{\rho}_{\alpha,\beta}(\lambda) = a^{1/2}\bar{\hat{\psi}}(a\lambda)\hat{f}(\xi(\lambda,\alpha,\beta))$ along the radial line $\lambda \in (-\infty,\infty)$, where $\hat{f}(\xi)$ is the 3D Fourier transform of $f(\mathbf{r})$. $a^{1/2}\bar{\hat{\psi}}(a\lambda)$ may be regarded as a window in the frequency domain. Therefore, the computation of surfacelet coefficients can be done efficiently by: (1) 3D fast fourier

transform (FFT) of $f(\mathbf{r})$ to obtain $\hat{f}(\xi)$; (2) radial sampling of $\hat{f}(\xi)$ along the radial line by varying λ with a fixed angular combination of (α,β) to form a new Radon domain of (λ,α,β); (3) applying the window function $a^{1/2}\overline{\hat{\psi}}(a\lambda)$ to each 1D Radon radial domain $(\cdot,\alpha,\beta)$ for a particular angle; and (4) finally applying the 1D inverse FFT to each one of the filtered 1D Radon domains.

For cylindrical surfacelets in Eqn.(0.5) and ellipsoidal surfacelets in Eqn.(0.6), the coefficients are not as simple as in Eqn.(0.13). But we still can compute based on Eqn.(0.12) in the frequency domain, where $\overline{\hat{\psi}}_{a,b,\alpha,\beta}(\xi)$ is viewed as a generic window function.

4 DUAL-REP MULTISCALE HETEROGENEOUS MODEL

Based on the proposed surfacelet basis functions, we model complex and multiscale geometries in an implicit form for multi-materials representation and analysis. The material distributions or concentrations are first specified explicitly at a finite number of positions. Then the distributions within the domain can be interpolated based on selected basis functions.

We are interested in modeling both internal and boundary distributions in a multiscale and multi-resolution representation. As mentioned in Section 2.2.3, wavelets are efficient in representing one-dimensional point singularities but not two- or three-dimensional ones. In contrast, surfacelets are efficient in two- or three-dimensional singularities but not one-dimensional ones. Therefore, a combination of wavelet and surfacelet basis functions is chosen. Wavelet basis functions are used for continuous internal distributions, while surfacelet basis functions are used for boundary distributions.

The dual-Rep model is illustrated schematically in Fig. 4. A grid is introduced and the corresponding nodal values are fixed in the modeling space. Nodes in the grid serve as points at which geometry and material compositions are sampled. They serve as the centers of references for wavelet and surfacelet functions, each of which has a scope of local support. Given some sampled values of material properties f_i at the nodes $\mathbf{r}_i$ in a grid space Ω, where $i=1,\ldots,n$, we can approximate material properties within Ω as

$$f(\mathbf{r}) = \sum_{i=1}^{n} f_i \left(\sum_{a_j} \sum_{b_k} \sum_{\mathbf{p}_l} c^{(i)}_{a_j,b_k,\mathbf{p}_l} \psi^{(i)}_{a,b,\mathbf{p}}(\mathbf{r}-\mathbf{r}_i) \right) \tag{0.14}$$

where a_j, b_k, $\mathbf{p}_l$ are the respective discretized parameter values of a, b, $\mathbf{p}$ in Eqn.(0.3). When the sampled nodes $\mathbf{r}_i$'s (denoted by "○" in Fig. 4) are within the internal region, we choose the bases in Eqn.(0.14) as regular wavelet tensor products as $\psi^{(i)}_{a,b,\mathbf{p}}(\mathbf{r}-\mathbf{r}_i) = \psi^{(i)}_{a,b}(x-x_i)\psi^{(i)}_{a,b}(y-y_i)\psi^{(i)}_{a,b}(z-z_i)$ without directional information. But when the sampled nodes (denoted by "●") are close to boundaries, we choose $\psi^{(i)}_{a,b,\mathbf{p}}(\mathbf{r}-\mathbf{r}_i)$ in Eqn.(0.14) to be the surfacelet functions.

In this dual-Rep model, wavelets have rectangular supports in capturing distributions. In contrast, surfacelets have the support of long and ellipsoidal shapes. With the combination of wavelets and surfacelets, we can approximate property distributions efficiently for both internal and boundary regions. In an interactive design environment, if designers specify the material properties f_i at the nodes $\mathbf{r}_i$'s (9 nodes in the example of Fig. 4), and the shapes of the basis functions associated these nodes $\psi^{(i)}_{a,b,\mathbf{p}}(\mathbf{r}-\mathbf{r}_i)$, the property distribution f within the domain then can be determined.

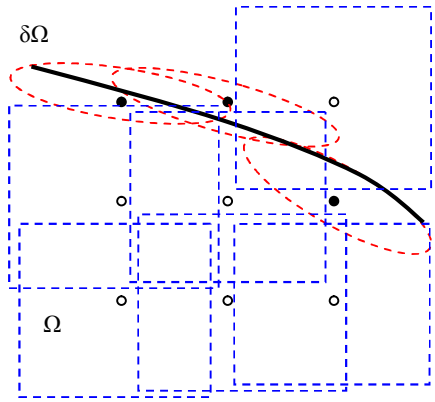

Fig. 4: Wavelet and surfacelet support illustrated in a 2D space.

4.1 An Example of Dual-Rep Model

Fig. 5 shows a simple example of dual-Rep models in 3D space with a combination of wavelet and surfacelet basis functions. The colored isosurfaces indicate the distribution of two materials, ranging from red to green. There are 27 grid points in the domain. Two of the grid points ($i = 1,27$) are associated with ellipsoidal surfacelets (labeled by "•"), whereas the others are with regular wavelets (labeled by "○"). Both functions are based on the Mexican hat basis in Eqn.(0.7) where $\sigma = 0.5$, and the distribution function is

$$\begin{aligned} f(x,y,z) = & \sum_{i=2}^{26} f_i \left(c_{a,b}^{(i)} a^{-3/2} \psi\left(a^{-1}\left[x - x_i\right]\right) \psi\left(a^{-1}\left[y - y_i\right]\right) \psi\left(a^{-1}\left[z - z_i\right]\right)\right) \\ & + f_1 c_{a,b}^{(1)} a^{-1/2} \psi\left(a^{-1}\left[0.25\left(z - z_1\right)^2 + \left(y - y_1\right)^2 + 4\left(x - x_1\right)^2 \right]\right) \\ & + f_{27} c_{a,b}^{(27)} a^{-1/2} \psi\left(a^{-1}\left[0.25\left(x - x_{27}\right)^2 + \left(y - y_{27}\right)^2 + 4\left(z - z_{27}\right)^2 \right]\right) \end{aligned} \tag{0.15}$$

where $b = 0$, $\alpha^{(1)} = \alpha^{(27)} = 0$, $\beta^{(1)} = \pi/2$, $\beta^{(27)} = 0$, $c_{a,b}^{(i)} = \sigma^3\sqrt{2\pi/a}$ $(i = 1,\ldots,27)$. The material property values at the nodes are listed in Tab. 1 with rows and columns corresponding to the positions in Fig. 5.

Fig. 5 shows the isosurfaces of the distributions with different scale factors ($a = 8,4,2,1,0.5,0.25$). It can be seen that the distributions are relatively smooth for large scale factors, since there are significant overlaps between support regions of basis functions. As the scale factor gradually reduces, the grid points become more "isolated islands". As a result, the scale factor provides direct controls in multiscale and multi-resolution modeling. The zoom operations based on the scale factor are introduced in Section 4.2.

4.2 Zoom-In Operations with Multiple Scales

A multiscale model should support zoom-in operations such that geometric, material, and property models at different size scales can be seamlessly integrated. When the designer zooms to a closer view of a region using the zoom-in operator, the number of grid points, and therefore the grid resolution, increases locally. In contrast to multi-resolution representations where the same model is used at different levels of resolution, a multiscale representation uses different models. The zoom-in process requires that a separate model is introduced to approximate local properties at a smaller scale.

There are two steps in building new models at a finer scale. One is choosing new grid points and values, the other is choosing new basis functions. In choosing new grid points and values, we can use

different subdivision rules. For instance, if the Catmull-Clark scheme is applied, the property value of the inserted node will be the weighted average of neighboring nodes, and the weights are based on topological relationships with its neighbors. Based on users' specifications, interpolating subdivision schemes can be chosen for *hard constraint* on grid point values, whereas approximating schemes can be applied for *soft constraint*.

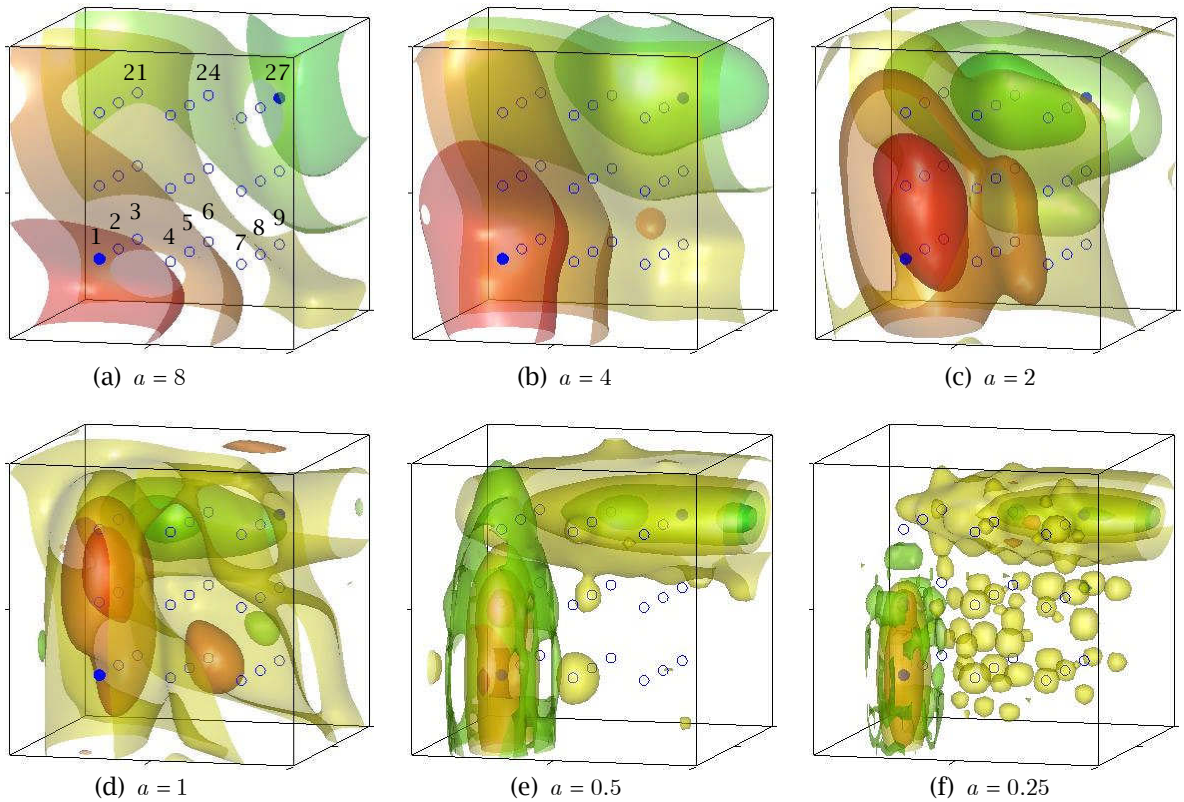

(a) $a = 8$ (b) $a = 4$ (c) $a = 2$

(d) $a = 1$ (e) $a = 0.5$ (f) $a = 0.25$

Fig. 5: Isosurfaces of material distributions in Eqn.(0.15) with different scales.

$f_{19} = 0.2, f_{20} = -0.2, f_{21} = -0.4$	$f_{22} = 0.1, f_{23} = -0.4, f_{24} = -0.6$	$f_{25} = -0.3, f_{26} = -0.5, f_{27} = -1.0$
$f_{10} = 0.8, f_{11} = 0.2, f_{12} = -0.1$	$f_{13} = 0.5, f_{14} = 0.2, f_{15} = -0.4$	$f_{16} = 0.2, f_{17} = -0.1, f_{18} = -0.6$
$f_1 = 1.0, f_2 = 0.5, f_3 = 0.1$	$f_4 = 0.6, f_5 = 0.4, f_6 = -0.2$	$f_7 = 0.3, f_8 = 0.2, f_9 = -0.4$

Tab. 1: Material values specified at the grid points in Fig. 5.

In choosing new basis functions for a different model, we need to find those bases that are suitable for both the newly inserted and original nodes for the new model at a more detailed level, depending on the nature of subdomains. Mapping procedures are needed to generate new models. For mappings from continuous domain to continuous domain, choosing new basis functions is straightforward. The same wavelets with different scales can be used. Similarly, for boundary to boundary mapping, the same surfacelets are applied. The complexity lies in the cases of continuous to boundary and boundary to continuous mappings. Continuous to boundary mappings occur when internal boundaries/interfaces emerge, such as in the transition from Fig. 1-(a) to Fig. 1-(c). Conversely, boundary to continuous mappings occur in transitions such as the one from Fig. 1-(a) to Fig. 1-(b), when internal boundaries disappear or are smoothed out with a finer LOD.

For the case of soft constraints, each step of the zoom-in process has wavelet or surfacelet interpolation involved. When a subdomain is chosen, new grid points in the subdomain need to be specified. For each new grid point, the property value is kept the same as in the previous scale. More formally, suppose that at the j-th scale the property distribution within its domain $\mathbb{D}_j$ is

$$f^{(j)}(\mathbf{r}) = \sum_{i=1}^{n_j} f_i^{(j)} \left(\sum_{a_j} \sum_{b_k} \sum_{\mathbf{p}_l} c_{a_j,b_k,\mathbf{p}_l}^{(i,j)} \psi_{a,b,\mathbf{p}}^{(i,j)} \left(\mathbf{r} - \mathbf{r}_i^{(j)} \right) \right) \qquad \left(\mathbf{r} \in \mathbb{D}_j \right)$$

We would like to find a new model

$$f^{(j+1)}(\mathbf{r}) = \sum_{i=1}^{n_{j+1}} f_i^{(j+1)} \left(\sum_{a_j} \sum_{b_k} \sum_{\mathbf{p}_l} c_{a_j,b_k,\mathbf{p}_l}^{(i,j+1)} \psi_{a,b,\mathbf{p}}^{(i,j+1)} \left(\mathbf{r} - \mathbf{r}_i^{(j+1)} \right) \right) \qquad \left(\mathbf{r} \in \mathbb{D}_{j+1} \right)$$

within a subdomain $\mathbb{D}_{j+1} \subset \mathbb{D}_j$ such that a distance function

$$\mathcal{S}_s = \int_{\mathbb{D}_{j+1}} \left[f^{(j+1)}(\mathbf{r}) - f^{(j)}(\mathbf{r}) \right]^2 d\mathbf{r} \tag{0.16}$$

is minimized, given that the property values at the new grid points $\mathbf{r}_i^{(j+1)}$'s are

$$f_i^{(j+1)} = f^{(j)} \left(\mathbf{r}_i^{(j+1)} \right) \qquad \left(i = 1, \ldots, n_{j+1} \right)$$

The necessary condition of optimality is

$$\frac{\partial \mathcal{S}_s}{\partial c_{a_j,b_k,\mathbf{p}_l}^{(i,j+1)}} = 2 \int_{\mathbb{D}_{j+1}} \left[f^{(j+1)}(\mathbf{r}) - f^{(j)}(\mathbf{r}) \right] f_i^{(j+1)} \psi_{a,b,\mathbf{p}}^{(i,j+1)} \left(\mathbf{r} - \mathbf{r}_i^{(j+1)} \right) d\mathbf{r} = 0 \quad \left(\text{for all } a,b,\mathbf{p},i \right)$$

That is

$$\sum_{i'=1}^{n_{j+1}} \sum_{a'} \sum_{b'} \sum_{\mathbf{p}'} f_{i'}^{(j+1)} \left[\int_{\mathbb{D}_{j+1}} \psi_{a',b',\mathbf{p}'}^{(i',j+1)} \left(\mathbf{r} - \mathbf{r}_{i'}^{(j+1)} \right) \psi_{a,b,\mathbf{p}}^{(i,j+1)} \left(\mathbf{r} - \mathbf{r}_i^{(j+1)} \right) d\mathbf{r} \right] c_{a',b',\mathbf{p}'}^{(i,j+1)} = \int_{\mathbb{D}_{j+1}} f^{(j)}(\mathbf{r}) \psi_{a,b,\mathbf{p}}^{(i,j+1)} \left(\mathbf{r} - \mathbf{r}_i^{(j+1)} \right) d\mathbf{r} \tag{0.17}$$

$$\left(\text{for all } a,b,\mathbf{p},i \right)$$

This linear system can be solved efficiently if the number of grid points and the levels of discrete $a,b,\mathbf{p}$ values are reasonable and the support of wavelet basis functions is localized.

For the case of hard constraints, the values of the smaller scale model at some specified positions $\mathbf{r}_g$ ($g = 1,2,\ldots$) have to exactly match those of larger scale model. The distance function becomes

$$\mathcal{S}_h = \int_{\mathbb{D}_{j+1}} \left[f^{(j+1)}(\mathbf{r}) - f^{(j)}(\mathbf{r}) \right]^2 d\mathbf{r} + \sum_g \lambda_g \left[f^{(j+1)}(\mathbf{r}_g) - f^{(j)}(\mathbf{r}_g) \right] \tag{0.18}$$

where λ_g's are the Lagrange multipliers that convert the constrained optimization problem to a non-constrained one. The necessary condition of optimality then is

$$\begin{cases} \int_{\mathbb{D}_{j+1}} \left[f^{(j+1)}(\mathbf{r}) - f^{(j)}(\mathbf{r}) \right] f_i^{(j+1)} \psi_{a,b,\mathbf{p}}^{(i,j+1)} \left(\mathbf{r} - \mathbf{r}_i^{(j+1)} \right) d\mathbf{r} + f_i^{(j+1)} \sum_g \lambda_g \psi_{a,b,\mathbf{p}}^{(i,j+1)} \left(\mathbf{r}_g - \mathbf{r}_i^{(j+1)} \right) = 0 \quad \left(\text{for all } a,b,\mathbf{p},i \right) \\ f^{(j+1)}(\mathbf{r}_g) = f^{(j)}(\mathbf{r}_g) \quad \left(\text{for all } g \right) \end{cases}$$

or

$$\begin{cases} \sum_{i'=1}^{n_{j+1}} \sum_{a'} \sum_{b'} \sum_{\mathbf{p}'} f_{i'}^{(j+1)} \left[\int_{\mathbb{D}_{j+1}} \psi_{a',b',\mathbf{p}'}^{(i',j+1)} \left(\mathbf{r} - \mathbf{r}_{i'}^{(j+1)} \right) \psi_{a,b,\mathbf{p}}^{(i,j+1)} \left(\mathbf{r} - \mathbf{r}_{i}^{(j+1)} \right) d\mathbf{r} \right] c_{a',b',\mathbf{p}'}^{(i,j+1)} + f_i^{(j+1)} \sum_g \psi_{a,b,\mathbf{p}}^{(i,j+1)} \left(\mathbf{r}_g - \mathbf{r}_i^{(j+1)} \right) \lambda_g \\ \qquad = \int_{\mathbb{D}_{j+1}} f^{(j)}(\mathbf{r}) \psi_{a,b,\mathbf{p}}^{(i,j+1)} \left(\mathbf{r} - \mathbf{r}_i^{(j+1)} \right) d\mathbf{r} \qquad (\text{for all } a,b,\mathbf{p},i) \\ \sum_{i'=1}^{n_{j+1}} \sum_{a'} \sum_{b'} \sum_{\mathbf{p}'} f_{i'}^{(j+1)} \psi_{a',b',\mathbf{p}'}^{(i',j+1)} \left(\mathbf{r}_g - \mathbf{r}_{i'}^{(j+1)} \right) c_{a',b',\mathbf{p}'}^{(i,j+1)} = f^{(j)}(\mathbf{r}_g) \qquad (\text{for all } g) \end{cases} \tag{0.19}$$

Fig. 6 is a simple one-dimensional example to illustrate the zoom-in operation. The original model is

$$f(x) = \sum_{i=1}^{5} f_i \left(c_{a,b}^{(i)} a^{-1/2} \psi \left(a^{-1} \left[x - x_i - b \right] \right) \right)$$

with $a = 0.25$, $b = 0.0$, $c_{a,b}^{(i)} = 0.5$, $\{x_i\} = \{-1.0, -0.5, 0.0, 0.5, 1.0\}$ and the corresponding $\{f_i\} = \{1.0, 0.5, 0.1, -0.5, -1.0\}$, and $\psi(\cdot)$ is the Mexican hat wavelet in Eqn.(0.7) with $\sigma = 0.73615$. Fig. 6-(a) shows the original model, where blue circles denote the grid points x_i's and values f_i's. Applying the soft constrained zoom-in operation to a subdomain $[-0.5, 0.0]$ and solving Eqn.(0.17), we obtain a smaller scale model as shown in Fig.6-(b), where the blue circles indicate the new grid points in the smaller scale. Notice that the actual model values at the grid points do not necessarily match the specified ones in the soft constrained cases. If hard constraints are applied on two boundary points of the subdomain as indicated by the red circles in the original model as in Fig. 6-(c), we obtain the new small scale model of Fig. 6-(d) by solving Eqn.(0.19). Fig. 6-(f) is a different small scale model when hard constraints are imposed on all five new grid points as shown in the original model in Fig. 6-(e). In all three small scale models, the same grid points are chosen. The respective coefficients of the resultant small scale models are listed in Tab. 2.

Fig. 7 is a three-dimensional example of zoom-in operation. The original model is shown in Fig. 7-(a). When 1/64 of the domain is selected to represent details, a smaller scale model as shown in Fig. 7-(b) is built based on Eqn.(0.19) with 27 constraining grid points.

5 MODEL RECONSTRUCTION

Besides direct specification of distributions in multiscale materials modeling, it is also desirable that models can be reconstructed from existing materials in the sense of reverse engineering. Dual-Rep models can be reconstructed from images of nano- or micro-structures. We can use nano- and micro-scale images such as those from atomic force microscopy and electron microscopy to characterize a material's structure. The boundaries of grains or phases can be detected from the images. In addition, the shading and its gradients in the images provide the information of material distributions. Given that calibration of images is done in the pre-processing step, a mapping from shading in images to properties can be achieved. In Section 3, we have shown that reconstruction of surfacelet models based on the Fourier transform is possible. In this section, we take a different surfacelet transform approach for model reconstruction.

A slightly different view of the surfacelet transform is that the surfacelet coefficients can be obtained by Radon alike transforms. As illustrated in Fig. 8-(a), the Radon transform in a domain Ω is the integral along the plane (represented as the dash line in 2D), which is perpendicular to a line with an angle. The plane and the line intersect at a point which has the radial distance of μ from the origin.

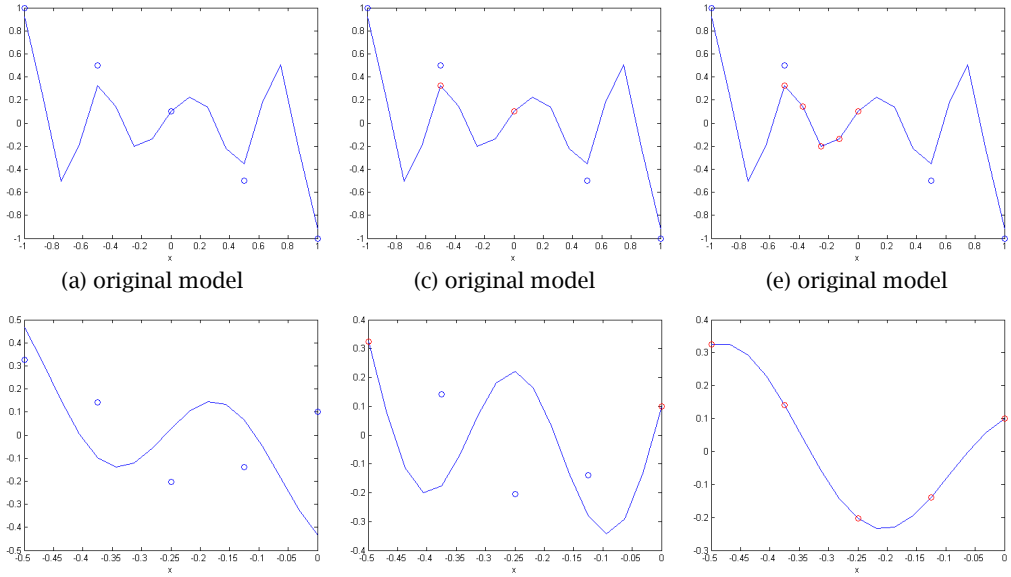

(a) original model (c) original model (e) original model

(b) small scale model (soft constrained) (d) small scale model (hard constrained at 2 (f) small scale model (hard constrained at 5

Fig. 6: A one-dimensional example to illustrate the zoom-in operations.

Original Model	Zoom-In Model		
Coefficients of Scale 1:	Unconstrained	Constrained grid points	Constrained grid points
		$x_1 = -0.5$	$x_1 = -0.5, x_2 = -0.375$
		$x_2 = 0.0$	$x_3 = -0.25, x_4 = -0.125, x_5 = 0.0$
$c^{(1,1)}_{0.25,0} = 0.5$	Scale 2 Coefficients	Scale 2 Coefficients	Scale 2 Coefficients
$c^{(2,1)}_{0.25,0} = 0.5$	$c^{(1,2)}_{0.25,0} = 1.5022$	$c^{(1,2)}_{0.25,0} = 3.7684$	$c^{(1,2)}_{0.25,0} = 0.3399$
$c^{(3,1)}_{0.25,0} = 0.5$	$c^{(2,2)}_{0.25,0} = -3.0225$	$c^{(2,2)}_{0.25,0} = -12.7689$	$c^{(2,2)}_{0.25,0} = 0.6465$
$c^{(4,1)}_{0.25,0} = 0.5$	$c^{(3,2)}_{0.25,0} = -1.0954$	$c^{(3,2)}_{0.25,0} = -11.8930$	$c^{(3,2)}_{0.25,0} = 0.4175$
$c^{(5,1)}_{0.25,0} = 0.5$	$c^{(4,2)}_{0.25,0} = -0.7581$	$c^{(4,2)}_{0.25,0} = 12.7573$	$c^{(4,2)}_{0.25,0} = -0.0813$
	$c^{(5,2)}_{0.25,0} = -2.7790$	$c^{(5,2)}_{0.25,0} = 11.0067$	$c^{(5,2)}_{0.25,0} = 0.7037$

Tab. 2: The example of zoom-in operation in Fig. 6.

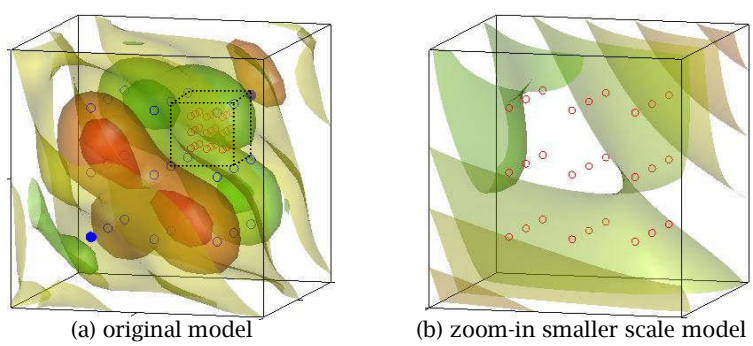

(a) original model (b) zoom-in smaller scale model

Fig. 7: A three-dimensional zoom-in operation example.

Varying the radius μ results in a vector of integral values $I_{\alpha,\beta}(\mu)$ with some specific angles α and β. That is,

$$I_{\alpha,\beta}(\mu) = \iiint f(x,y,z)\,\delta(x\cos\beta\cos\alpha + y\cos\beta\sin\alpha + z\sin\beta - \mu)\,dx\,dy\,dz \tag{0.20}$$

where δ is the Dirac delta function. The ridgelet transform then is the 1D wavelet transform of the surface integral values $I_{\alpha,\beta}(\mu)$ on the plane as in

$$\Psi_{a,b,\alpha,\beta} = \left\langle I_{\alpha,\beta}(\mu), \psi_{a,b}(\mu) \right\rangle \tag{0.21}$$

In general, our generic surfacelet transform is the 1D wavelet transform of the surface integrals. For the cylindrical surfacelet in Eqn.(0.5), the surface integral is

$$I_{\alpha,\beta,r_0,r_1,r_2}(\mu) = \iiint f(x,y,z)\,\delta\begin{pmatrix} r_1(\cos\beta\cos\alpha\cdot x + \cos\beta\sin\alpha\cdot y + \sin\beta\cdot z - \mu)^2 \\ +r_2(-\sin\alpha\cdot x + \cos\alpha\cdot y)^2 - r_0^2 \end{pmatrix} dx\,dy\,dz \tag{0.22}$$

For the ellipsoidal surfacelet in Eqn.(0.6), the integral is

$$I_{\alpha,\beta,r_0,r_1,r_2,r_3}(\mu) = \iiint f(x,y,z)\,\delta\begin{pmatrix} r_1(\cos\beta\cos\alpha\cdot x + \cos\beta\sin\alpha\cdot y + \sin\beta\cdot z - \mu)^2 \\ +r_2(-\sin\alpha\cdot x + \cos\alpha\cdot y)^2 \\ +r_3(-\sin\beta\cos\alpha\cdot x + \sin\beta\sin\alpha\cdot y + \cos\beta\cdot z)^2 - r_0^2 \end{pmatrix} dx\,dy\,dz \tag{0.23}$$

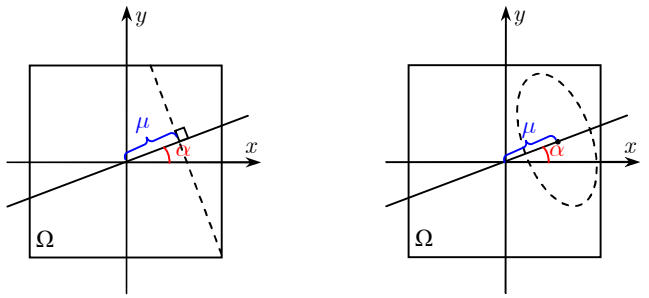

(a) ridgelet transform

(b) cylindrical and ellipsoidal surfacelets

Fig. 8: Geometric interpretations of parameters in surfacelet transforms.

The materials model can be reconstructed from images based on the surfacelet transform defined by Eqns.(0.20)-(0.23). The process of computing surfacelet coefficients from 3D images is illustrated in Fig. 9. From a 3D materials distribution, the surface integrals on surfacelets are calculated and arranged in a 3D matrix with μ, α, and β as indices. Then 1D wavelet transforms along the μ axis direction are performed for all α's and β's. The results are surfacelet coefficients for a particular angle.

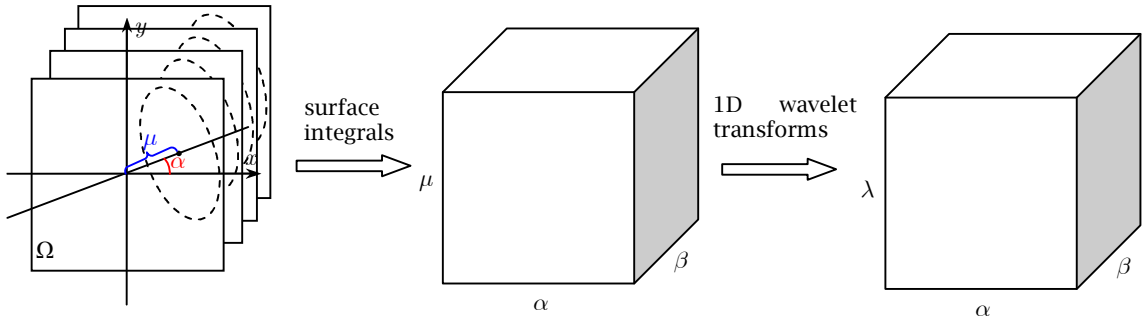

Fig. 9: The general process of surfacelet transforms.

From scanning electron microscope (SEM) images of SiO2-MnO2 based ceramics [33] shown in Fig. 10-(a), the material model can be reconstructed based on the surfacelet transform. Fig. 10-(b) shows the examples of surface integrals based on the 3D ridgelet in Eqn.(0.4), where different colors denote the magnitudes. The dominant grain boundary orientations can be easily identified. Fig.10-(c) shows the surfacelet coefficients after the wavelet transform. Here, the Haar wavelet is used. The low-pass coefficients are stored in the upper half of the 3D matrix, whereas high-pass coefficients are in the lower half. Some fine details and local features are revealed in the high-pass coefficients.

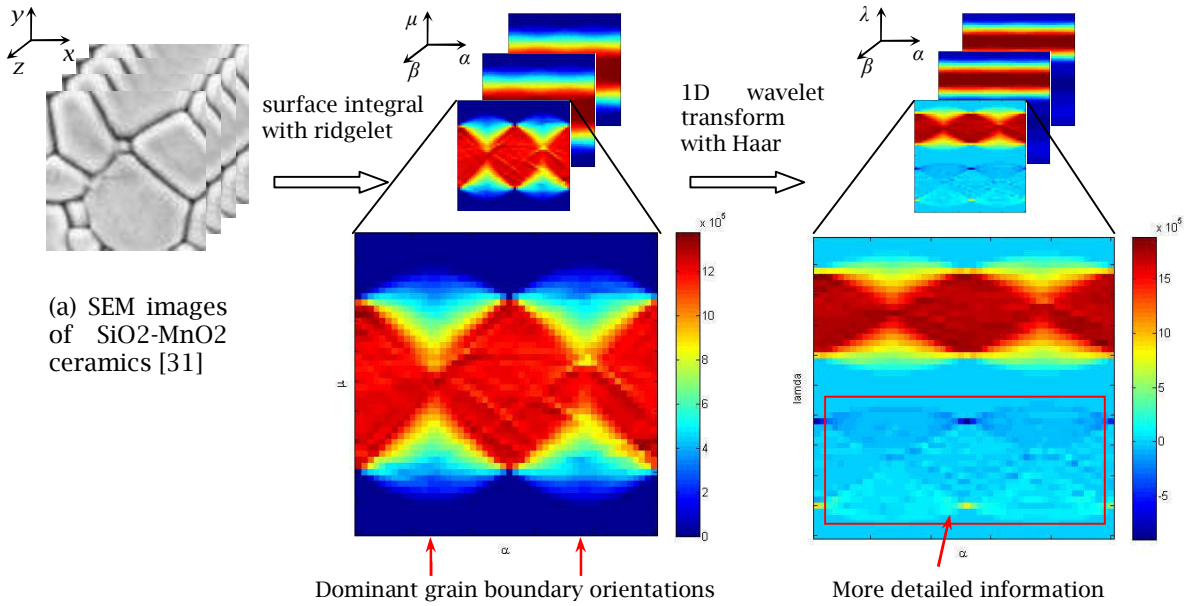

(a) SEM images of SiO2-MnO2 ceramics [31]

(b) wedgelet surface integral

(c) surfacelet coefficients

Fig. 10: An example of materials model reconstruction based on 3D ridgelet.

As a second example to illustrate, a model of polyacrylonitrile-based nanofibers [34] can be reconstructed based on the cylindrical surfacelet. The SEM images are shown in Fig. 11-(a). The original 3D images in the Euclidean space thus are transformed to the reciprocal space. The examples of surface integrals are shown in Fig. 11-(b). The surfacelet coefficients are in Fig. 11-(c), as in Eqn.(0.5). Here, the parameters of the cylindrical surfacelet are $r_1 = r_2 = 1$ and radius $r_0 = 0.66$. The centers of circular nanofibers can be easily located from the surface integrals and coefficients. Notice that not

only the original material model with the largest number of $\psi^{(i)}_{a,b,\mathbf{p}}$'s in Eqn.(0.14) can be used, lower resolution models are also readily available, where the number of $\psi^{(i)}_{a,b,\mathbf{p}}$'s is reduced by cutting off those terms with small coefficients.

6 SUMMARY

In this paper, we introduce a new multiscale heterogeneous representation, dual-Rep, to support computational geometry and materials design. The dual-Rep model represents both internal and boundary distributions with a unified implicit form. Surfacelets as new basis functions are proposed to capture boundary information, which are more efficient than the traditional wavelets, whereas wavelets are used to represent internal distributions. With the unified basis functions, zoom-in operations are developed to enable interactive multiscale specifications. Surfacelet transform allows surfacelet coefficients to be directly computed from images in model reconstruction.

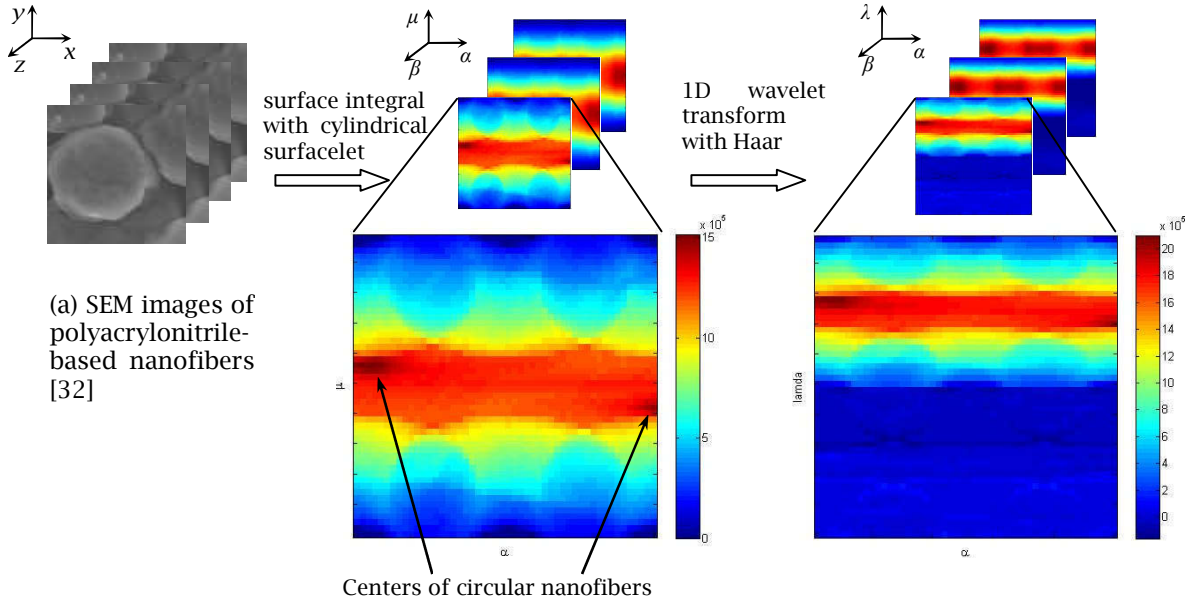

(a) SEM images of polyacrylonitrile-based nanofibers [32]

(b) cylindrical surface integrals

(c) surfacelet coefficients

Fig. 11: An example of materials model reconstruction based on cylindrical surfacelets.

REFERENCES

[1] Rosen, D. W.: Thoughts on hierarchical modeling methods for complex structures, Computer-Aided Design & Applications, 6(3), 2009, 419-430.

[2] Kou, X. Y.; Tan, S. T.: Heterogeneous object modeling: A review, Computer-Aided Design, 39(4), 2007, 284-301.

[3] Bhashyam, S.; Shin, K. H.; Dutta, D.: An integrated CAD system for design of heterogeneous objects, Rapid Prototyping Journal, 6(2), 2000, 119-135.

[4] Koenig, O.; Fadel, G.: Application of genetic algorithms in the design of multi-material structures manufactured in rapid prototyping, Proc. Solid Freeform Fabrication Symposium, pp. 209-217, Austin, TX, August 9-11, 1999.

[5] Wu, Z. W.; Soon, S. H.; Feng, L.: NURBS-based volume modeling, International Workshop on Volume Graphics, 321-330, 1999.

[6] Adzhiev, V.; Kartasheva, E.; Kunii, T.; Pasko, A.; Schmitt, B.: Hybrid cellular-functional modeling of heterogeneous objects, ASME Journal of Computing and Information Science in Engineering, 2, 2002, 312-322.
[7] Kumar, V.; Burns, D.; Dutta, D.; Hoffmann, C.: A framework for object modeling, Computer-Aided Design, 31, 1999, 541-556.
[8] Liu, H.; Maekawa, T.; Patrikalakis, N.M.; Sachs, E.M.; Cho, W.: Methods for feature-based design of heterogeneous solids, Computer-Aided Design, 36, 2003, 1141-1159.
[9] Tan, S. T.; Siu, Y. K.: Source-based heterogeneous solid modeling, Computer-Aided Design, 44(1), 2002, 41-55.
[10] Ganter, M.; Wahlborg, J.; Schwartz, D.; Storti, D.: H-ISM: An implementation of heterogeneous implicit solid modeling, Proc. ASME Design Automation Conference, paper #DETC2002/DAC-34139, Montreal, Sept 29 – Oct. 2, 2002.
[11] Rvachev, V. L.; Sheiko, T. I.; Shapiro, V.; Tsukanov, I.: Transfinite interpolation over implicitly defined sets, Computer Aided Geometric Design, 18, 2001, 195-220.
[12] Pratap, A.; Crawford, R. H.: Implementation of a functionally gradient material modeling and design system, Proc. Solid Freeform Fabrication Symposium, 150-161, Austin, TX, Aug. 4-6, 2003.
[13] Piegl, L.; Tiller, W.: Software engineering approach to degree elevation of B-spline curves, Computer-Aided Design, 26(1), 1994, 17-28.
[14] Catmull, E.; Clark, J.: Recursively generated B-spline surfaces on arbitrary topological meshes, Computer-Aided Design, 10, 1978, 350-355.
[15] Doo, D.; Sabin, M. A.: Behavior of recursive subdivision surfaces near extraordinary points, Computer-Aided Design, 10, 1978, 356-360.
[16] Loop, C.: Smooth subdivision surfaces based on triangles, Master's Thesis, University of Utah, 1987.
[17] Dyn, N.; Levine, D.; Gregory, J. A.: A butterfly subdivision scheme for surface interpolation with tension control, ACM Transactions on Graphics, 9(2), 1990, 160-169.
[18] Kobbelt, L.: $\sqrt{3}$ -subdivision, Proc. SIGGRAPH 2000, pp.103-112.
[19] Li, G.; Ma, W.; Bao, H.: $\sqrt{2}$ subdivision for quadrilateral meshes, Visual Computer, 20(2-3), 2004, 180-198.
[20] Chuang, G. C.-H.; Kuo, C.-C.J.: Wavelet descriptor of planar curves: theory and applications, IEEE Transactions on Image Processing, 5(1), 1996, 56-70.
[21] Daubechies, I.; Runborg. O.; Sweldens, W.: Normal multiresolution approximation of curve, Constructive Approximation, 20(3), 2004, 399-463.
[22] Wang, Y.-P.: Image representations using multiscale differential operators, IEEE Transactions on Image Processing, 8(12), 1999, 1757-1771.
[23] Wang, Y.-P.; Lee, S.L.; Toraichi, K.: Multiscale curvature-based shape representation using B-spline wavelets, IEEE Transactions on Image Processing, 8(11), 1999, 1586-1592.
[24] Donoho, D.: Wedgelets: nearly minimax estimation of edges, The Annals of Statistics, 27(3), 1999, 895-897.
[25] Candès, E.J.; Donoho, D.L.: Recovering edges in ill-posed inverse problems: optimality of curvelet frames, The Annals of Statistics, 30(3), 2002, 784-842.
[26] Candès, E. J.: Ridelets: theory and applications, Ph.D. dissertation, Standford University, 1998.
[27] Do, M. N.; Vetterli, M.: The contourlet transform: an efficient directional multiresolution image representation, IEEE Transactions on Image Processing, 14(12), 2005, 2091-2106.
[28] Donoho, D. L.; Huo, X.: Beamlets and multiscale image analysis. In T.J. Barth, T. Chan, and R. Haimes (Eds.), Multiscale and Multiresolution Methods: Theory and Applications, pp.149-196, 2001.
[29] Willett, R. M.; Nowak, R. D.: Platelets: a multiscale approach for recovering edges and surfaces in photon-limited medical imaging, IEEE Transactions on Medical Imaging, 22(3), 2003, 332-350.
[30] Ying, L.; Demanet, L.; Candès, E.: 3D discrete curvelet transform, Proc. SPIE Conf. Wavelet Applications in Signal & Image Processing, San Diego, CA, vol. 5914, pp.591413, 2005.
[31] Lu, Y. M.; Do, M. N.: Multidimensional directional filter banks and surfacelets, IEEE Transactions on Image Processing, 16(4), 2007, 918-931.

[32] Chandrasekaran, V.; Wakin, M.B.; Baron, D.; Baraniuk, R.G.: Representation and compression of multidimensional piecewise functions using surflets, IEEE Transactions on Information Theory, 55(1), 2009, 374-400.
[33] Orlandi, M. O.; Bueno, P. R.; Leite, E. R.; Longo, E.: Nonohmic behavior of SnO2.MnO2-based ceramics, Materials Research, 6(2), 2003, 279-283.
[34] Wu, S.; Zhang, F.; Hou, X.; Yang, X.: Stretching-induced orientation for improving the mechanical properties of electrospun polyacrylonitrile nanofiber sheet, Advanced Materials Research, 47-50, 2008, 1169-1172.